New Journal of Physics

The open access journal at the forefront of physics

PAPER

An investigation on THz yield from laser-produced solid density plasmas at relativistic laser intensities

S Herzer[1], A Woldegeorgis[1,2], J Polz[1], A Reinhard[1], M Almassarani[1,2], B Beleites[1,2], F Ronneberger[1,2], R Grosse[1,2], G G Paulus[1,2], U Hübner[3], T May[3] and A Gopal[1,2]

1   Institut für Optik und Quantenelektronik, Friedrich-Schiller-Universität Jena, Max-Wien-Platz 1, D-07743 Jena, Germany
2   Helmholtz Institut Jena, Fröbelstieg 3, D-07743 Jena, Germany
3   Leibnitz Institut für Photonische Technologien, Albert-Einstein-Strasse, D-07745 Jena, Germany
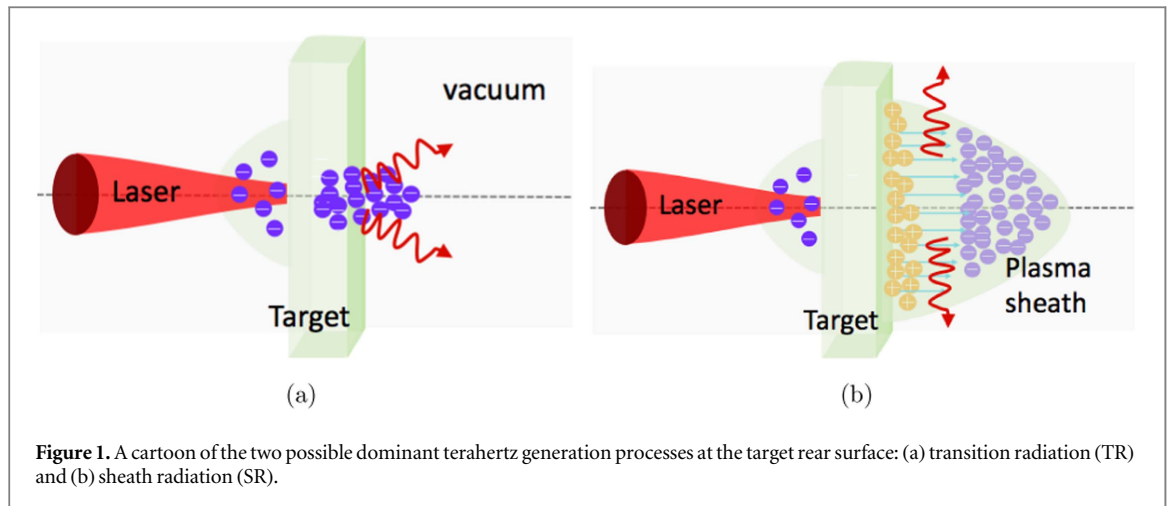
E-mail: amrutha.gopal@uni-jena.de

Abstract

We experimentally characterize the generation of high-power terahertz radiation (THz) at the rear surface of a target irradiated by multiple laser pulses. A detailed dependence of the THz yield as a function of laser pulse duration, energy, target material and thickness is presented. We studied the THz radiation emitted mainly in two directions from the target rear surface, namely target normal (acceptance angle 0.87 sr) and non-collinear direction (perpendicular to the target normal direction—acceptance angle 4.12 sr). Independent measurements based on electro-optic diagnostics and pyroelectric detector were employed to estimate the THz yield. Most of the energy is emitted at large angles relative to the target normal direction. THz yield increases with incident laser intensity and thinner targets are better emitters of THz radiation compared to thicker ones.

1. Introduction

High-power laser matter interaction has been a subject of extensive experimental and theoretical investigations over the last few decades. It has been effectively used to generate high frequency radiation [1], ultra large quasi-static electric and magnetic fields [2, 3], accelerated particle beams [4, 5] etc. In recent years we have witnessed a remarkable interest in utilizing this process for coherent terahertz generation [6–8]. This is due to the fact that the plasma produced during such an interaction has many advantages over other well established terahertz generation methods due to their compactness, high damage threshold and high conversion efficiency [7]. In the last decade terahertz radiation has attracted great interest, thanks to the availability of compact optical source which could generate THz radiation with greater efficiency compared to the electronic sources. Terahertz radiation has the advantage over other wavelengths due to their low photon energy which allows the radiation to penetrate though materials with out altering the material properties [9] and the associated electric and magnetic fields can be employed to coherently control matter and influence the spin dynamics in magnetic materials [10–17]. Furthermore, characterization of the radiation also provides invaluable insight into the spatio-temporal dynamics of the generation process [18–20]. Thus, increase in demand of sources has led to numerous studies which explored the possibility to generate broadband as well as monochromatic terahertz sources in a multitude of schemes [6, 21]. Among the currently available compact and high-power pulsed terahertz sources, short-pulse laser based schemes are the most efficient. Table-top short-pulse lasers are tested workhorses of todays university scale laboratories. Interaction of these focused laser pulses with matter in solid or gaseous form can easily ionize the matter and generate plasmas whose dynamics is affected by the properties of the interacting laser pulse as well as the medium. For many applications such as, high-harmonic generation, ion acceleration etc [22] solid targets are preferred over the gaseous ones. Indeed in the case of terahertz generation also solid targets have the upper edge due to high electron density and low re-absorption etc.

Figure 1. A cartoon of the two possible dominant terahertz generation processes at the target rear surface: (a) transition radiation (TR) and (b) sheath radiation (SR).

2. THz generation at the target rear surface

During laser–solid interaction, terahertz radiation is generated from the target front (interaction) and rear surface. Unlike terahertz emission from the target front surface where the NIR laser pulse interacts with the solid foil, the generation of coherent terahertz radiation from the rear surface is different. In the case of emission from the target front surface, there are a multitude of physical processes responsible for terahertz generation from the laser-plasma interaction region [23–28] which are directly dependent on the incident laser parameters (polarization, ASE contrast, pulse duration, intensity) and target material etc. However, in the case of emission from the rear surface [7, 8, 29–34] the THz dynamics has to depend on the hot electrons which are generated at the front surface during the interaction of laser pulse with the foil and gain energy and accelerated back to the target ballistically, travel through the target and exit the rear surface. This electron dynamics subsequently generates a strong charge separation field comparable to the peak electric field of the laser pulse, resulting in the ionization of the hydrocarbon impurities at the rear surface and accelerating the positive charges to very high energies. With currently available laser intensities, this is the main mechanism of ion acceleration and is also called sheath acceleration process [35–39]. Fundamental laws of electromagnetism tell us that transient motion of charge particles leads to emission of electromagnetic radiation [40]. This radiation can be coherent and or incoherent due to the collective and individual motion of the charged particles. Further, the spectra of the radiation depend on the energy and temporal characteristics of the particle bunch. In summary, one can identify mainly two dominant processes (figure 1) which could lead to coherent emission from the target rear surface, namely transition radiation (TR) and sheath radiation (SR). At the outset, is the TR due to the fast electrons exiting the target rear surface [41]. Next is the SR due to the transient dynamics of the plasma sheath formed at the target rear surface which accelerates the positive charges.

However for understanding the experimental results presented here we discuss the above mentioned processes briefly. During laser-thin foil interaction, the electron energy spectra observed both in experiments and simulations have quasi-thermal distribution and can be calculated from the ponderomotive potential of the incident laser pulse [39]. Thus the thermal energy $k_B T_e$ of the hot electrons generated at the target front surface can be written as [36]

$$k_B T_e = m_e c^2 \left[\left(1 + \frac{I_L \lambda_L^2}{1.37 \times 10^{18}} \right)^{\frac{1}{2}} - 1 \right] \tag{1}$$

where $m_e c^2$ is the rest mass energy of the electron, I_L the laser intensity (for a focal spot of radius r_0 and pulse duration τ_L and laser energy E_L) in W cm^{-2} and λ_L the central wavelength of the laser in microns respectively. The radial dimension of the electron bunch exiting the rear surface is r_{rear} and can be written as $r_{rear} = r_0 + d \cdot \tan \theta$, where d is the thickness of the target, θ is the half angle of electron emission and r_0 is the radius of the laser focus at the front surface. Based on the experimental parameters ($r_0 = 2 \ \mu$m, $d = 5 \ \mu$m, $\theta = 10°$), we can calculate the total number of electrons ($N_B \simeq \eta E_L / k_B T_e$) accelerated into the target for the duration of the incident laser pulse and exited at the target rear surface to form plasma sheath. First let us consider the case of TR generated by the electrons exiting the target rear surface.

TR generation in the optical and high frequency regime during high-power laser plasma interaction is well studied both experimentally and theoretically [41–47] and the angular distribution of the emission is very close to the target normal direction. However, TR can also be generated in the long wavelength or THz regime. The energy distribution of the hot electrons generated during laser-plasma interaction is broad and close to
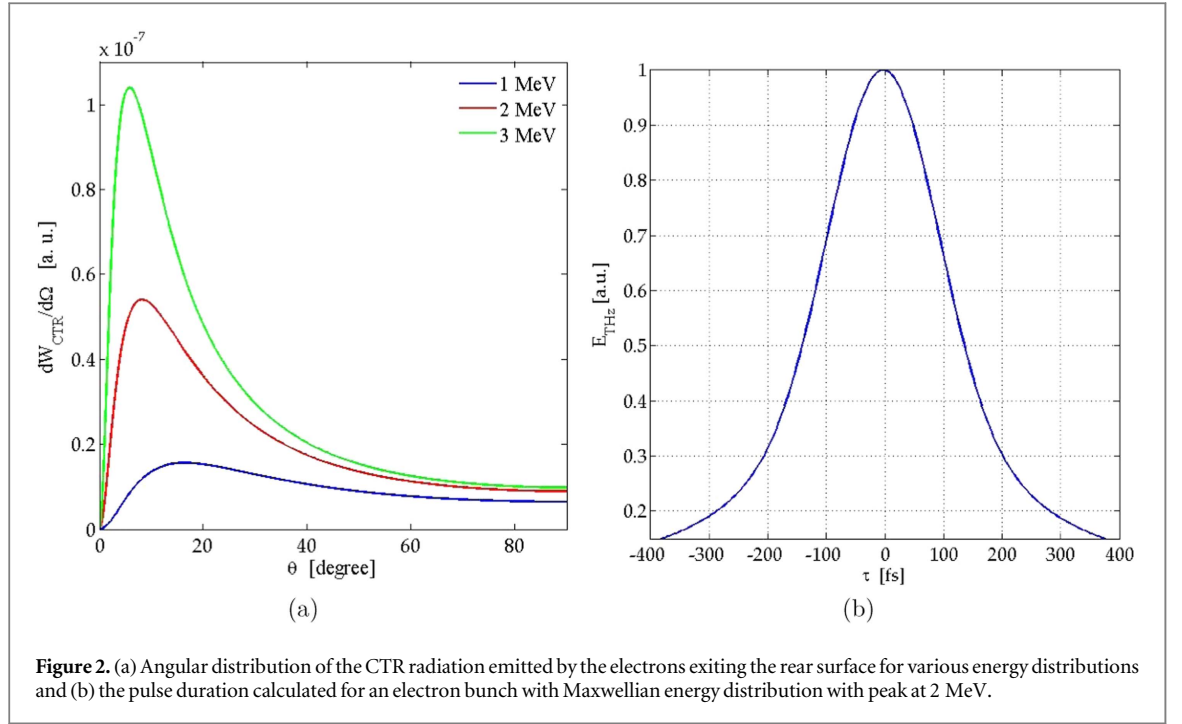
Figure 2. (a) Angular distribution of the CTR radiation emitted by the electrons exiting the rear surface for various energy distributions and (b) the pulse duration calculated for an electron bunch with Maxwellian energy distribution with peak at 2 MeV.

Boltzmann distribution [35, 36]. The radiation emitted per unit solid angle per unit angular frequency by the particle bunch crossing the boundary is given by
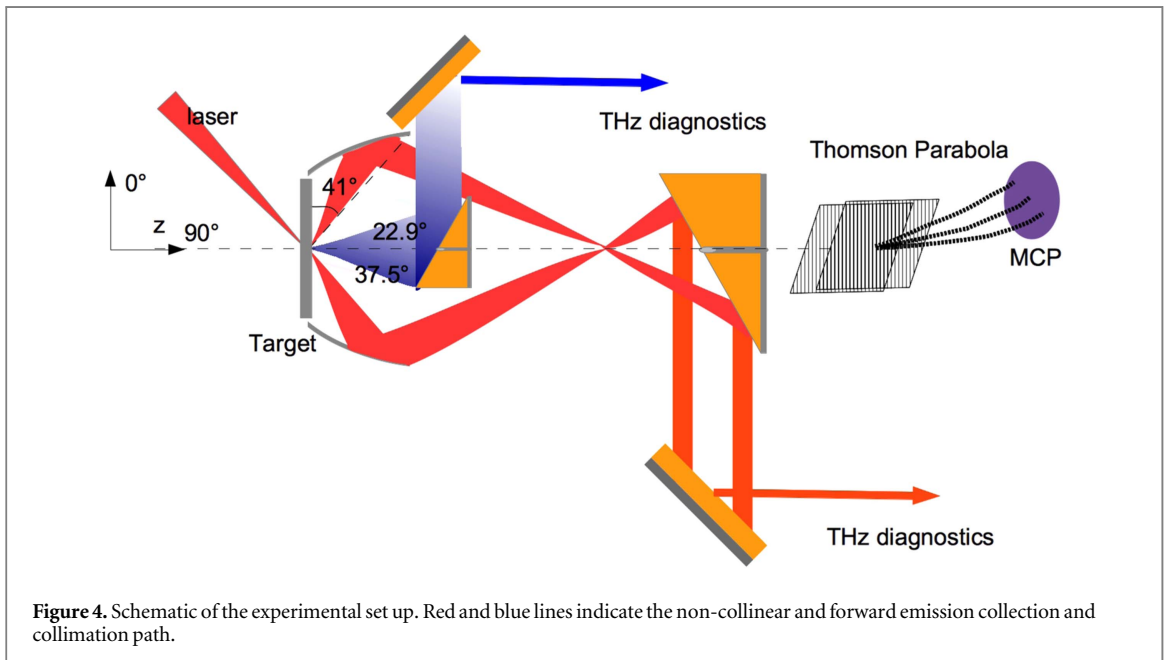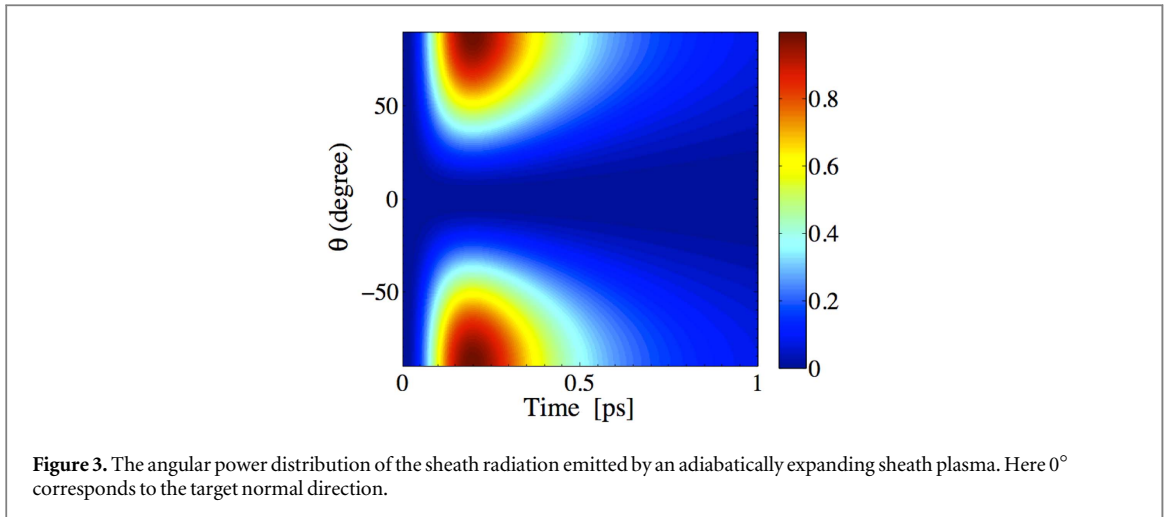
$$\frac{d^2W}{d\omega d\Omega} = \frac{e^2 N_B}{\pi^2 c}\left[\int d^3\mathbf{p}(\mathcal{E}_\parallel^2 + \mathcal{E}_\perp^2) + (N_B - 1)\left(\left|\int d^3\mathbf{p}f(\mathbf{p})\mathcal{E}_\parallel\mathcal{F}\right|^2 + \left|\int d^3\mathbf{p}f(\mathbf{p})\mathcal{E}_\perp\mathcal{F}\right|^2\right)\right], \quad (2)$$

where $f(p)$ is the momentum distribution function and N_B is the number of the electrons in the bunch. $\mathcal{F}$ is the coherence function and $\mathcal{E}_\parallel$ and $\mathcal{E}_\perp$ are the Fourier transforms of the electric field in the parallel and perpendicular radiation plane. First term on the right-hand-side is the incoherent spectral density (Incoherent TR or ITR) and the second term is the coherent spectral density (CTR). The ITR is proportional to the number of the electrons N_B in the bunch summarized over individual particle contribution. ITR is independent of radiation frequency ω and is just a function of emission angle θ. However, here we take into consideration only the coherent emission due to the following reasons. Firstly, the electron bunch length (σ_z) is shorter than the wavelength λ of the emitted radiation. We assume further that the electrons are generated only during the wake of the laser pulse, i.e. for a pulse duration of $\tau_L = 30$ fs corresponds to a longitudinal bunch dimension of $\sigma_z = c\tau_L \sim 9$ μm, then the terahertz radiation generated below 30 THz should be coherent. Secondly, the incoherent emission (ITR) is many orders of magnitude ($\propto N_B$) weaker than the coherent radiation ($\propto N_B^2$). The CTR spectrum depends on both the particle momentum distribution **p** and the bunch form factor $\mathcal{F} = \mathcal{F}_\parallel\mathcal{F}_\perp$ in transverse ($\mathcal{F}_\perp(p)$) and longitudinal ($\mathcal{F}_\parallel(z)$) directions. Figure 2(a) shows the directionality of the radial electric field created by the simulated charge distribution of electron bunch for our laser parameters exiting the target rear surface. The emission peaks at small angles with respect to the target normal direction (0°). Temporal duration of the emission for an electron bunch with 2 MeV peak energy is 274 fs (figure 2(b)).

The second mechanism which could give rise to coherent terahertz radiation is the sheath acceleration process that generates and accelerates the protons and ions to MeV energies (figure 1(b)). A simple description of this process could be as follows. The hot electrons exiting the target rear surface excites a strong charge-separation field (sheath field). This field is strong enough to field ionize the neutral atoms at the rear surface and accelerates the positive charges forward in the target normal direction until they catch up with the electrons in the sheath front and co-propagate further. Thus the transient dynamics of the sheath field governed by the ion motion give rise to strong non-collinear emission in the terahertz range. [7, 29, 30]. The radiation emitted by the transient dynamics of the plasma sheath field can be calculated using the Liénard–Wiechert potential [40]

$$\mathbf{E}_{THz}(\mathbf{r}, t) = \frac{1}{4\pi\epsilon_0}\int(d\mathbf{r}')\left\{\frac{\mathbf{n}}{cr}\frac{\partial}{\partial t}[\rho(\mathbf{r}', t')]_{ret} \cdots \cdots - \frac{1}{c^2 r}\frac{\partial}{\partial t}[\mathbf{J}(\mathbf{r}', t')]_{ret}\right\}, \quad (3)$$

where, the source terms on the right hand side are the spatio-temporal distributions of the charge density ρ ($\rho(z, t) = e[n_e(z, t) - n_p(z, t)]$) and plasma current **J** ($\mathbf{J}(\mathbf{r}, t) = -e\mathbf{v}_f(t)\delta(z)\rho(z, t)\mathbf{e}_z$) which are calculated for the incident laser intensities using the plasma expansion model [36]. Substituting the source terms for the nonlinear wave equation we can calculate the energy flux per unit time, given by Poynting's vector $\mathbf{S}(\mathbf{r}, t) = \frac{c}{4\pi}\mathbf{E}(\mathbf{r}, t) \times \mathbf{B}(\mathbf{r}, t)$. The angular distribution of emitted radiation power for an incident laser

Figure 3. The angular power distribution of the sheath radiation emitted by an adiabatically expanding sheath plasma. Here 0° corresponds to the target normal direction.

Figure 4. Schematic of the experimental set up. Red and blue lines indicate the non-collinear and forward emission collection and collimation path.

intensity $I_{L} \sim 10^{19}\,\mathrm{W\,cm^{-2}}$ is plotted in figure 3 and is evident that the radiation is emitted at large angles to the target normal direction implying dipole like radiation pattern. Here an initial electron temperature $k_{B}T_{e} = 2\,\mathrm{MeV}$ and a density $n_{e} = 5 \times 10^{19}\,\mathrm{cm^{-3}}$ [48] leads to a pulse duration $\tau \approx 400\,\mathrm{fs}$.

The two terahertz radiation generation processes have different angular emission patterns and temporal durations depending on the electron temperature. For example for an electron temperature of 2 MeV, the angular distribution of TR is close to the target normal peaking at $\sim 15°$ (figure 1(a)) while in the case of SR the emission the emission peaks at 90°. Indeed the low energy electrons ($< 2\,\mathrm{MeV}$) escaping the rear surface and generating TR will have an angular distribution similar to the one generated by the plasma expansion. However, they will be emitted at different time frames with respect to the interaction. In addition to the above mentioned processes, other effects may also generate terahertz radiation coherently and incoherently during laser-plasma interaction, such as electron-reflexes at the target rear surface and plasma thermal emission etc. However, those contributions are insignificant compared to the CTR and SR due to the fact that the latter are emitted coherently within the time scale comparable to the incident laser pulse and also their spatial origin is very small compared to the wavelength of emission.

In this paper we present a detailed experimental study on THz emission from the target rear surface. Measurements were carried out for THz radiation in the target normal and non collinear directions as depicted in figure 4 below.

3. Experimental setup

The experiments were carried out at the JETI (JEna Ti-Sapphire) laser facility at the Institute of Optics and Quantum Electronics at the University of Jena. A schematic of the experimental setup is shown in figure 4. JETI delivers 30 fs (FWHM) duration pulses at 800 nm central wavelength, which were focused using 45° f/1.2 off-axis parabola to $10 \pm 0.4 \, \mu m^2$ (FWHM) area generating intensities $\geqslant 5 \times 10^{19}$ W cm^{-2}. Thin foil targets consisting of Titanium (5 μm), Aluminum (2–10 μm), Copper (5 μm), Gold (5 μm) or CH (6.5 μm) were used for terahertz generation. The foil targets were stretched using deep cooling and slow expansion technique and mounted onto 5 cm diameter Aluminum rings. The target holder rims were 5 mm broad so that the radiation emitted from the front side of the target was blocked from entering the collection optics. Terahertz radiation generated at the target rear surface were collected in two geometries. We define 0° and 90° corresponds to target surface and target normal respectively. In the non-collinear direction (0° + 41° & 180° − 41°) a modified ellipsoidal mirror was employed. The entrance or front side of the mirror was sectioned to let the interaction laser shine on the target. The target was placed at the first focal point of the ellipsoidal mirror which was also the focus of the OAP. The target normal direction and major axis of the ellipse lie on the same plane. The radiation emitted from the target rear surface was collected by the ellipsoidal mirror and was focused down to the second focal point of the ellipse which lies at 24.1 cm from the first focal point along the major axis. The radiation was then collimated using a 3 inch off-axis parabola (with a 3 mm hole in the middle to let the ion beam through) and steered out of the experimental vacuum chamber through a High Resistive Float Zone Silicon (HRFZ-Si) or a TPX window using metallic mirrors. The collimated THz radiation was then focused down using a 4 inch off-axis parabolic mirror on to the THz diagnostics. THz radiation emitted in the forward direction (90° + 37.5° & 90° − 22.9°) was collected by replacing the ellipsoidal mirror with a 3 inch (f/1), 90° off-axis parabola. A 3 mm hole in the parabola allowed the simultaneous detection of the ion spectra. The asymmetrical collection angle of forward emission is due to the geometry of the collecting parabola. The solid angle of each observation region was estimated by taking into consideration the experimental geometry and it is calculated to be 4.21 sr and 0.87 sr respectively for non-collinear and forward directions.

3.1. THz diagnostics

Terahertz diagnostics consisted of a calibrated pyrometer operating at room temperature providing the actual energy of the THz pulse falling onto the detector head. The detector is made of LiTaO$_3$ crystal coated with black absorbing material having uniform response in the THz band. The detector was supplied with calibration curves for the spectral band 30–600 μm for the factory settings of the readout electronics. It was then re-calibrated at the host institute at wavelengths 30 μm, 532 nm, 800 nm and 1064 nm respectively. Calibrated bandpass filters placed in front of the entrance window of the detector provided additional spectrally resolved measurements. Silicon based broadband THz attenuators were inserted in the beam path to avoid saturation of the detector signal. Additionally, measurements were also taken with HRFZ silicon, Aluminum sheets and dry paper to test the leakage of any laser radiation onto the detector. Furthermore, the detector housing was grounded to avoid triggering of the acquisition system through electromagnetic impulses generated during the laser-matter interaction. Total terahertz yield was estimated by measuring the peak voltage on the pyroelectric detector multiplied by the transmittivity of the window and attenuators and calibration factor. For spectral measurements using bandpass filters, the spectral density of each bandpass filter was calculated for their respective bandwidth.

The THz radiation was further characterized by an independent, single-shot, non-collinear electro-optic (EO) pump-probe diagnostic. For this purpose, Gallium Phosphide (GaP) (100 μm thick) and Zinc Telluride (ZnTe) (500 μm thick) crystals cut in the ⟨110⟩ crystal plane were employed. The Pyrometer was replaced by the EO crystal at the focus of the THz beam. A schematic of the non-collinear EO diagnostic is shown in figure 5. The THz pulse incident normal to EO crystal generates transient birefringence in the x–y plane. Here we specify the incident plane as xy and the propagation direction as z axis. A portion (2%) of the main beam was splitted before the experimental chamber, collimated and temporally delayed using a remote controlled kinematic stage and sent at an angle to the EO crystal. Due to the geometry of the scheme one side of the optical beam arrives earlier at the EO crystal than the other end. Thus the temporal profile of the transient birefringence and hence, the temporal dynamics of the THz pulse on the EO crystal can be mapped onto the spatial profile of the optical pulse. The time window of the observation (T) is defined by the diameter (w) of the optical beam and the angle (α) subtended between the optical and THz pulse at the EO crystal [49].

$$T = \frac{w}{c} \tan(\alpha). \qquad (4)$$

Temporal resolution and time window were accurately measured by varying the delay of the probe pulse and observing the position of the image on the CCD camera, providing 33 fs and 9 ps respectively. Initially linearly
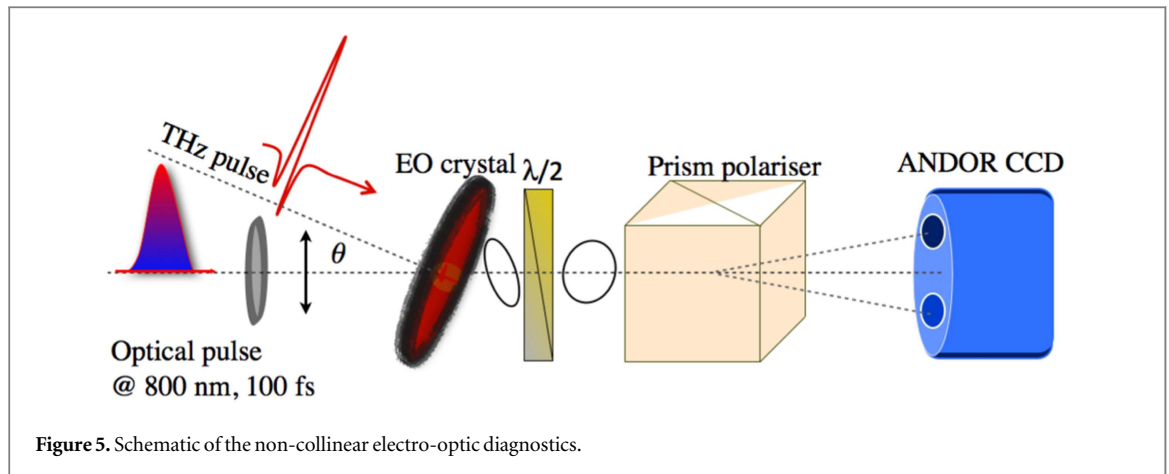
Figure 5. Schematic of the non-collinear electro-optic diagnostics.

polarized optical pulse is elliptically polarized after traveling through the EO crystal with THz pulse. The induced birefringence was measured using the balanced detection scheme [50]. The output signal of the balanced detection scheme is directly proportional to the THz electric field and its Fourier transform provides the spectral content. Inherent birefringence, absorption and velocity mismatch in the EO crystal were taken into consideration by estimating the crystal response function, which is divided in the Fourier domain to the detected signal and performing the inverse process while estimating the THz field strength and spectrum. However, the losses occurred in the THz transmission line is not taken into consideration. For a linearly polarized optical pulse the phase retardation induced is given by [50]

$$\Gamma(\theta) = \frac{n_0^3 r_{41} E_{\text{THz}} \sqrt{1 + 3\cos^2\theta}\,\omega d}{2c}, \tag{5}$$

where d is the thickness of the crystal, ω is the frequency of the optical probe pulse, θ is the angle between the electric field of the THz pulse and the $[-1, 1, 0]$ axis of the EO crystal, r_{41} and n_0 are the EO coefficient and refractive index of the crystal respectively.

As mentioned before, different types of crystals were employed for the EO detection measurements defined by the THz signal strength provided by the pyroelectric measurements. For the non-collinear measurements, the THz signal strength was high enough to generate strong birefringence in thinner crystals. However, for the forward emission, thicker crystal was needed to generate significant birefringence signal above the noise level. Hence, 100 μm thick GaP crystal was employed for NC measurements and 500 μm thicker ZnTe crystal was used for the FE measurements. However, this limited the bandwidth of the detected signal [50]. In figure 6 the crystal response function of each of the crystal type employed is presented and it is clear that high THz frequencies can be reached only with thinner crystals. In ZnTe crystal, the upper limit of detection is 4.5 THz due to lattice resonance. Thinner GaP crystals allowed higher frequency detection up to 9 THz.

3.2. Particle diagnostics
In addition to terahertz diagnostics proton and ion spectra from the target rear surface were also recorded simultaneously. The 3 mm hole on the collimating parabola (figure 4) enabled the simultaneous recording of the ion spectra. A classical ion spectrometer which employs parallel electric and magnetic fields to disperse the particles according to their energies and to deflect each species into specific trajectories defined by their energy and E and B field strength was deployed. The spectrometer was housed in a separate vacuum chamber attached to the main experimental chamber looking towards the target normal direction at the rear of the target. A lead and steel plate with 5 mm diameter aperture placed at the entrance of the spectrometer chamber collimated the particle beam. A second variable aperture placed behind the collimating aperture defined the energy resolution of the measurements. A micro channel plate (MCP) detector with phosphor screen and a CCD camera recorded the ion spectra for every laser shot. Calibration shots were taken by exposing *CR*—39 plastic by placing in front of the MCP detector. The plastic was later etched and counted the ion damaged pitches to estimate the exact number of particles of each species entering the spectrometer. More details on the spectrometer design and calibration are given in Schwoerer *et al* [51].

3.3. Laser diagnostics
The temporal pre-pulse contrast and the pulse duration were measured during the daily operation. The pulse energy is measured for every shot using a calibrated energy meter. The focal spot of the laser at the focus in vacuum was measured using a kinematic focal diagnostics which can be moved in and out of the beam path

Figure 6. EO response function of the various crystals employed in our measurements.
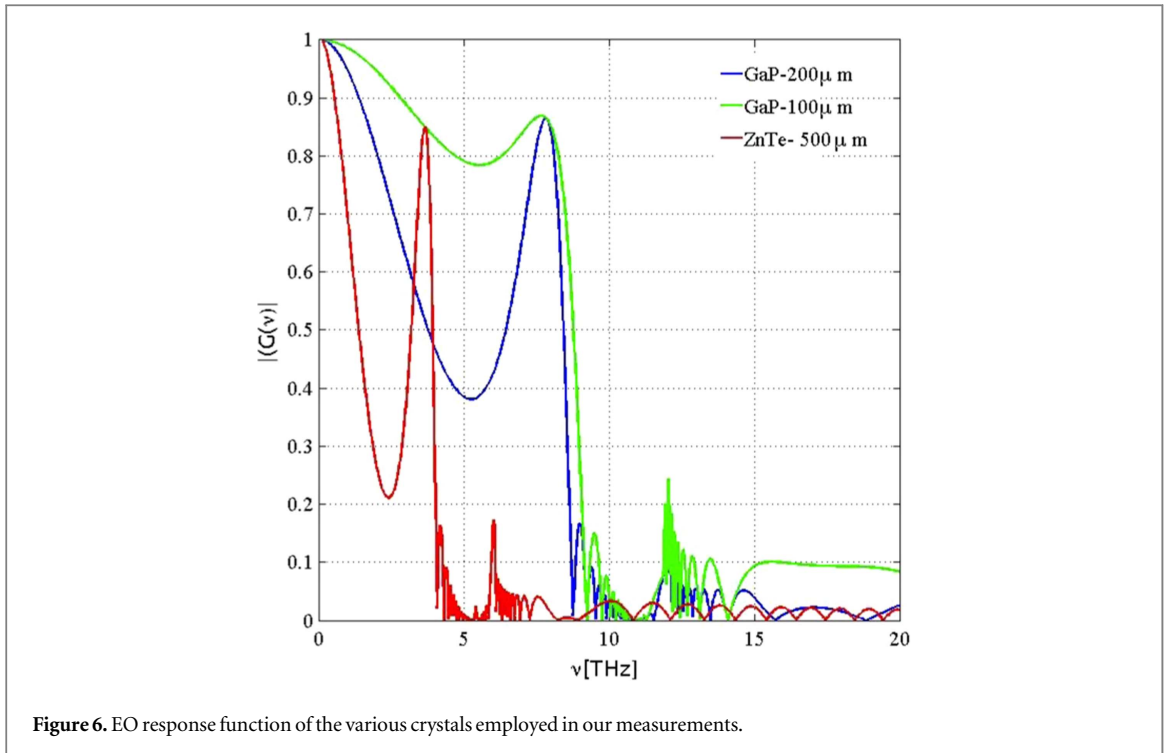
during the measurements. Adaptive mirrors were installed to optimize the beam profile and thereby the focal spot by iteratively changing the mirror voltages during daily operations. The foil targets were placed at the focal spot using an alignment Helium–Neon laser following the same beam path as the main beam after the last amplification stage. A x-ray dosimeter placed outside the vacuum chamber looking in the target normal direction along with the ion spectrometer enabled the optimization of the target focal position. The temporal contrast ($>10^{-3}$ with in 500 fs) and the pulse duration did not change significantly during the experimental campaign thereby affecting the proton spectrum and x-ray dose.

The results presented here are carried out in a series of experiments at the JETI laser facility. THz diagnostics, ion spectrometer and x-ray dosimeter were running in parallel during all the experimental measurements. Thereby, the THz measurements could be compared with the x-rays dose and ion spectra. During each measurements the laser conditions, such as temporal pulse contrast, energy, and pulse duration were also recorded daily. The humidity and temperature of the laboratory was also recorded thereby any absorption lines in the THz spectra could be taken into consideration.

4. Results and discussion

4.1. Spatio-temporal characterization of THz pulse

As mentioned in the previous section, the terahertz radiation generated at the target rear surface was measured for two regions, in the forward (FE or target normal direction—acceptance angle of 0.87 sr) and non-collinear direction (NC—perpendicular to the target normal direction—acceptance angle of 4.12 sr). For both arrangements, at first the space-time integrated energy was measured using the calibrated pyrodetector. Calibrated bandpass filters placed in front of the detector also provided an independent estimate of the spectral content of each measurements. Thereafter, the pyrodetector was replaced by the EO crystal to measure the temporal characteristics of the emission.

The space time integrated energy of the terahertz radiation measured for an incident laser pulse duration of 30 fs from a 5 μm thick Titanium foil was 712 and 40 μJ in non-collinear and forward directions respectively. This indicate that the FE is an order of magnitude weaker than the NC emission. If we assume that the radiation is emitted isotropically (i.e.TR due to hot electrons ($\leqslant 1$ MeV)) then one may compare the THz yields in both directions to their respective collection angles. Such an estimate would have resulted in the detection of at least a factor of 4 more in the forward direction. However, the experimental results based on two independent measurements presented in figure 9 indicate otherwise.

EO measurements provided the temporal dynamics of the THz pulses. Equation (5) states that the rotation induced is directly proportional to the crystal thickness d and r_{41}. The 100 μm thick GaP crystal ($r_{41} = 1$ pm V^{-1}) has a thickness five times less than ZnTe ($r_{41} = 4.5$ pm V^{-1}) and r_{41} factor of four times
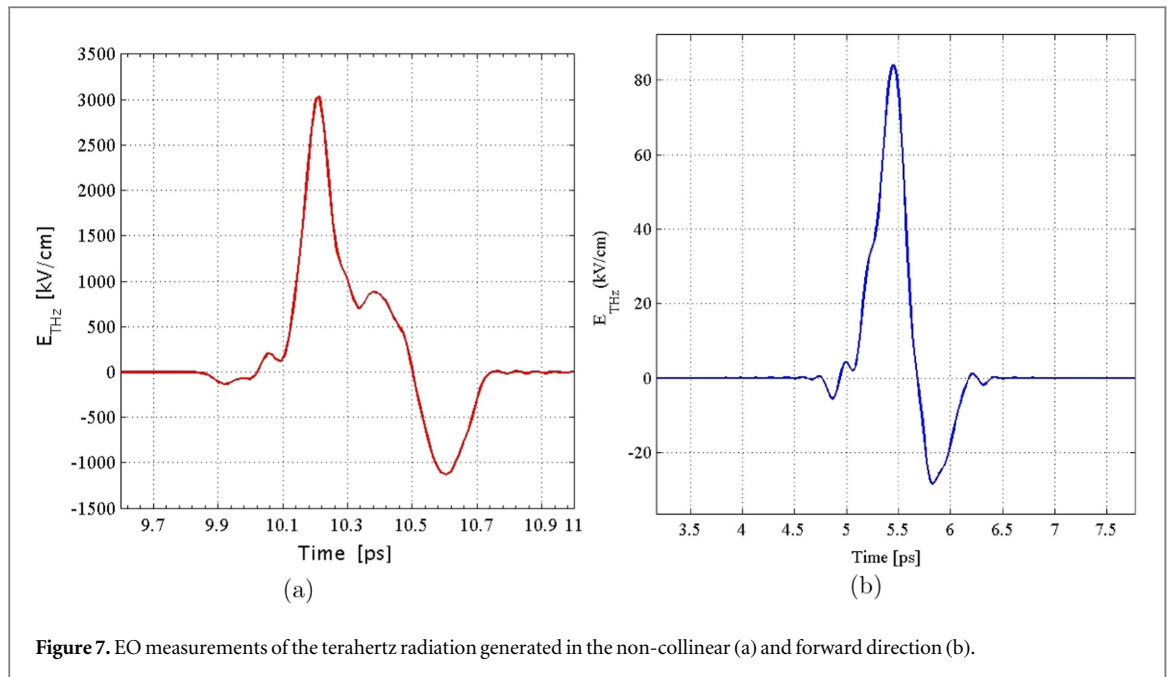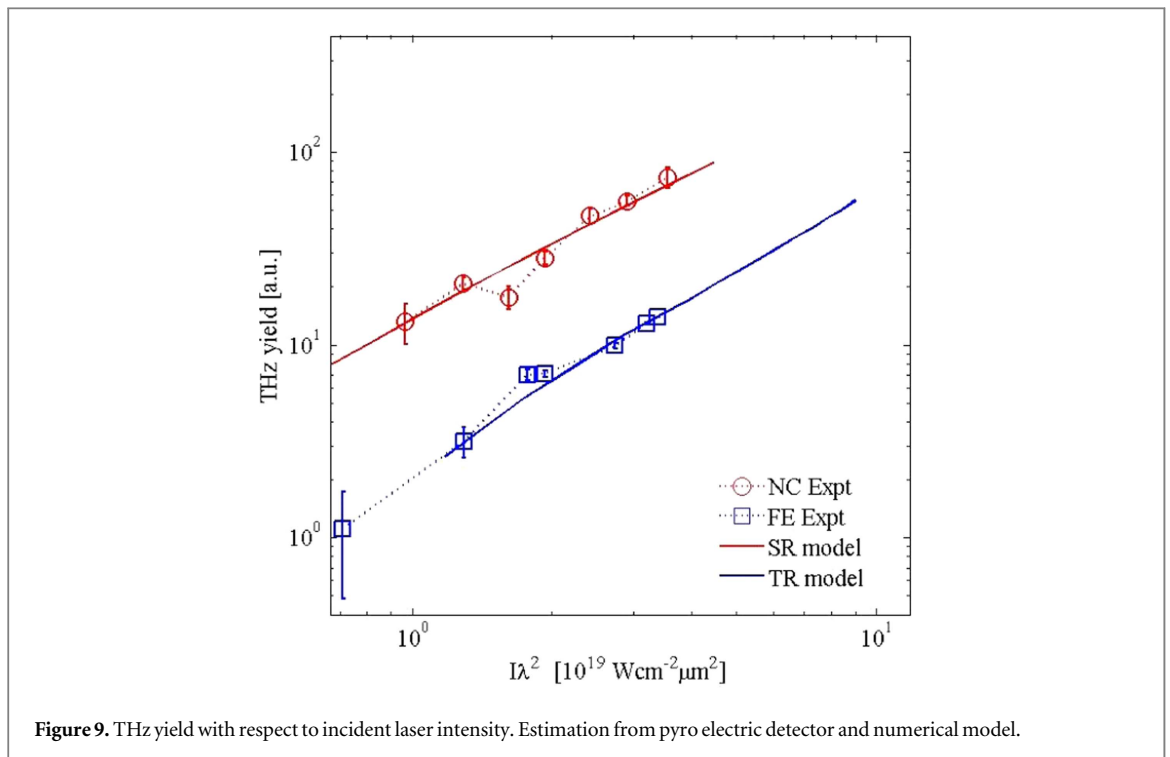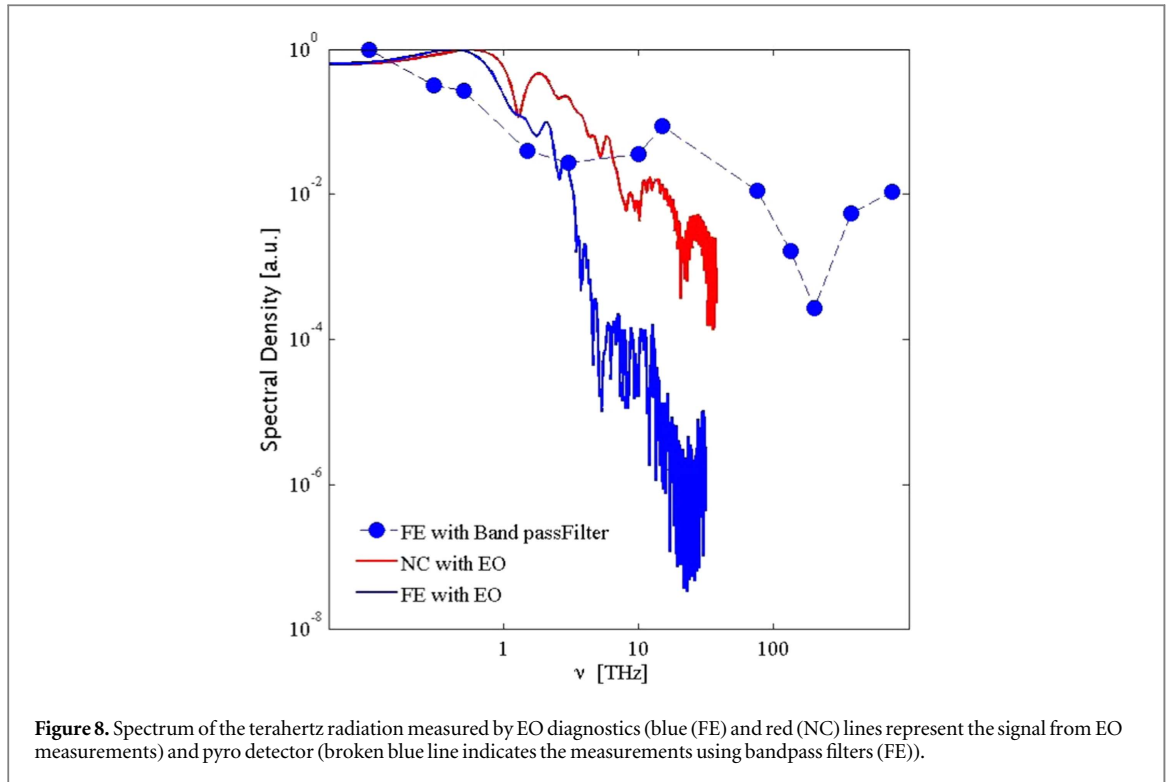
Figure 7. EO measurements of the terahertz radiation generated in the non-collinear (a) and forward direction (b).

smaller, the EO signal strength of NC is saturated compared to FE. Thus the FE field strength is at least two orders of magnitude smaller than NC, thereby confirming independently the measurements based on pyroelectric detector. The field strength of NC emission is saturated and thereby we measure the minimum field strength of 3 MV cm^{-1} in the NC direction. Based on the pyrometer data the field strengths could be above 100 MV cm^{-1} indicating the highest field strength of THz available in the laboratory for any scheme of generation. In the case of FE the field strength is only 86 kV cm^{-1}.

The temporal duration of the THz pulse is estimated from the electric field measurements. The signal from the EO detection scheme is Fourier transformed and divided by the crystal response function in the frequency domain to obtain the spectra and inverse transformed to obtain the electric field. The electric field results are presented in figure 7 and the corresponding spectral distribution is presented in figure 8. As mentioned before, the minimum temporal duration of the measurements are affected by the crystal function, which are calculated by taking into consideration, crystal thickness, velocity matching of THz and optical pulse in the crystal and the lattice oscillations (TO) in the crystal etc. The lowest TO frequency for ZnTe and GaP are 5.3 THz and 11 THz respectively, which sets the maximum THz frequencies that can be detected with a particular type of crystal. For the 500 μm ZnTe crystal, the highest level reachable was 3 THz, and for 100 μm GaP it was 9.3 THz (figure 7). FE measurements indicate that the duration of the THz pulse was 446 fs limited by the thicker ZnTe crystal. Based on the TR model and hot electron generation process by ponderomotive scaling, the duration should be around 274 fs for FE emission. However, due to the low TR signal thicker EO crystal was required for experimental verification which provided longer than theoretically expected value. For the 500 μm ZnTe crystal, the minimum measurable pulse duration is 330 fs. NC measurements show extremely strong and saturated THz pulse with $E_{THz} > 3$ MV cm^{-1}. Here we point out that the earlier measurements using 200 μm thick GaP crystal provided a pulse duration of $\tau_{THz} \sim 570$ fs. [30]. This suggests that the thinner crystal provided a more accurate value of the NC pulse duration. The spectral content of the THz pulses shown in figure 8. NC measurements suggest that radiation is broadband with spectral contents up to 9 THz and most of the energy is below 3 THz range. Spectral decay slope for FE is faster than the NC, indicating the emission process is due to the particle bunch escaping the rear surface (TR) whose momentum distribution is Maxwellian.

4.2. Dependence on incident laser energy and pulse duration

Firstly, we discuss the influence of incident laser intensity on SR and CTR yield. The laser intensity was varied by changing the laser energy while keeping the pulse duration and focal spot size the same. The results of experimental and numerical studies are plotted in figure 9. In the case of NC emission, the experimental data indicate that the THz yield increases with incident laser intensity and follows a scaling law of $(I\lambda^2)^{1.45 \pm 0.12}$, while the results from the SR model varies less steeply with a scaling law of $(I\lambda^2)^{1.3}$. The FE yield increases more similar to NC following a power law of $(I\lambda^2)^{1.45 \pm 0.13}$ and the TR model follows a power law of $(I\lambda^2)^{1.43}$. The small discrepancy (with in the error bars) between the experiment and model could be due to the error in fine adjustment of the collection optics, beam relay system and the focusing conditions. For the yield estimation in models we considered the geometrically measured solid angles for calculation. However, during experiments

Figure 8. Spectrum of the terahertz radiation measured by EO diagnostics (blue (FE) and red (NC) lines represent the signal from EO measurements) and pyro detector (broken blue line indicates the measurements using bandpass filters (FE)).

Figure 9. THz yield with respect to incident laser intensity. Estimation from pyro electric detector and numerical model.

there are more degrees of freedom than in numerical models. Even though the results from analytical models and experiential data agree well for FE and and NC within the error bars of measurements, further investigation is needed with more experiential data points with varying laser parameters.

Next, the laser pulse duration was varied from 30 to 90 fs thereby the incident intensity decreased from $5 - 1.6 \times 10^{19} \, \text{W cm}^{-2}$. As we can see from figure 10(b), the THz yield decreases for longer pulse duration, albeit less steeply compared to figure 9. Here the results are based on the EO measurements. This reduction in the signal strength can be attributed to the fact that as the pulse duration increases, the intensity on target decreases (figure 10(a)) and thereby the temperature of the hot electrons from 5.5 to 2 MeV. Even though the reduction in hot electron temperature is compensated by the increase in the number of hot electrons (from
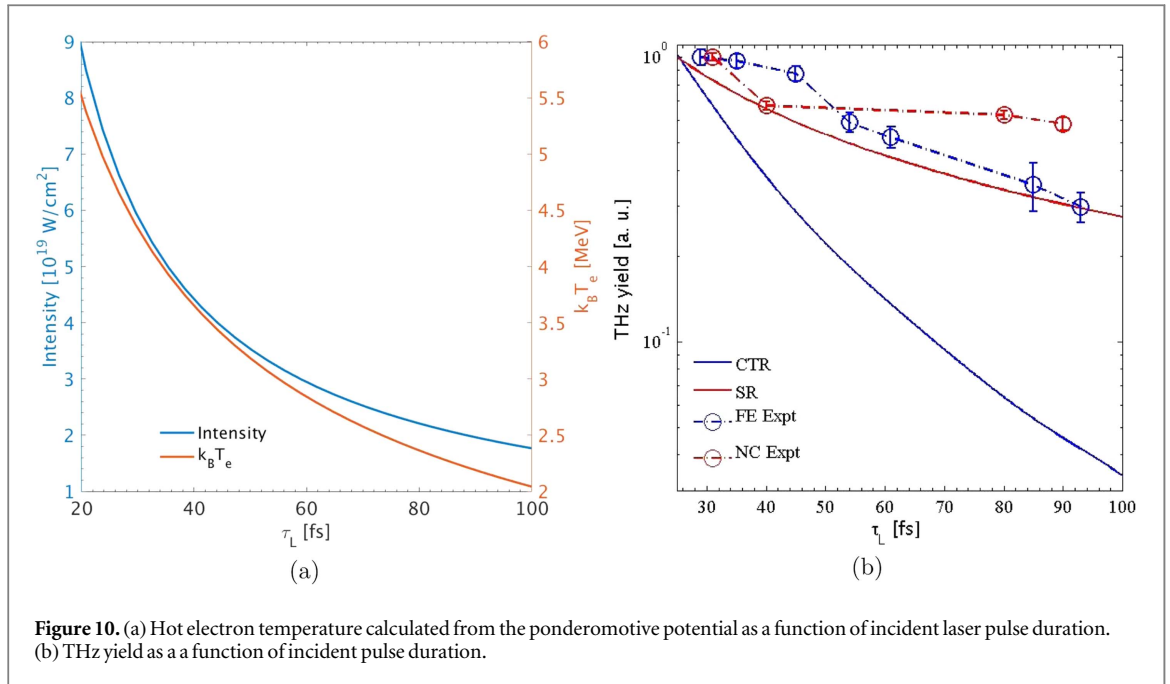
Figure 10. (a) Hot electron temperature calculated from the ponderomotive potential as a function of incident laser pulse duration. (b) THz yield as a a function of incident pulse duration.
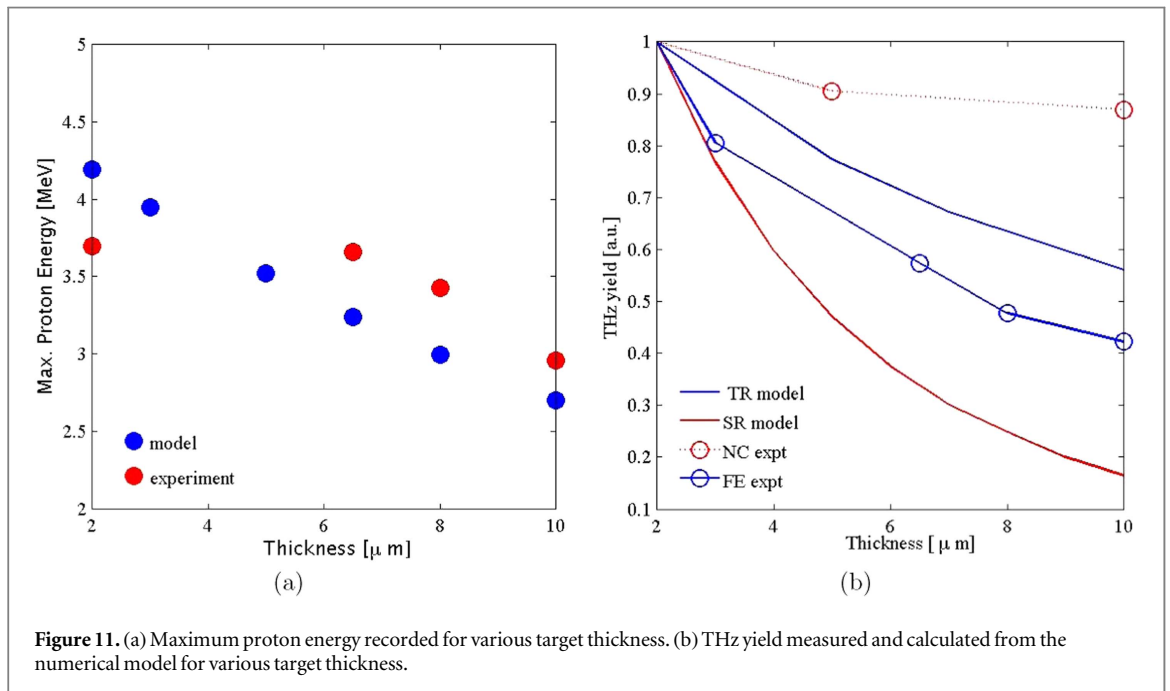

Figure 11. (a) Maximum proton energy recorded for various target thickness. (b) THz yield measured and calculated from the numerical model for various target thickness.

1.1×10^{11} to 3×10^{11}), the signal strength is greatly influenced by the electron momentum and thereby the temperature.

4.3. Dependence on target material and thickness

Similarly, the dependence of target thickness and target material on THz yield was investigated. Results presented in figure 11 point that, for the same material (Aluminum), thinner targets generate higher terahertz radiation irrespective of the generation mechanism. These results are compared with the maximum proton energy measured and estimated numerically [39]. Similar to proton acceleration, thinner targets generate higher peak energies resulting in stronger THz yields as the hot electrons endure less losses in the medium. Although this tendency predicts reduction in target thickness can yield higher THz, ultra thin targets may not be suitable as they can lead to mechanical instability and thereby generate lesser number of hot electrons [52].

Further studies based on different target materials indicate that thinner, low Z metallic foils are better candidate for generating THz compared to high-Z materials (figure 12(b)). Although, care must be taken in interpreting the data as the results are not obtained for the same thickness, where low Z materials show higher
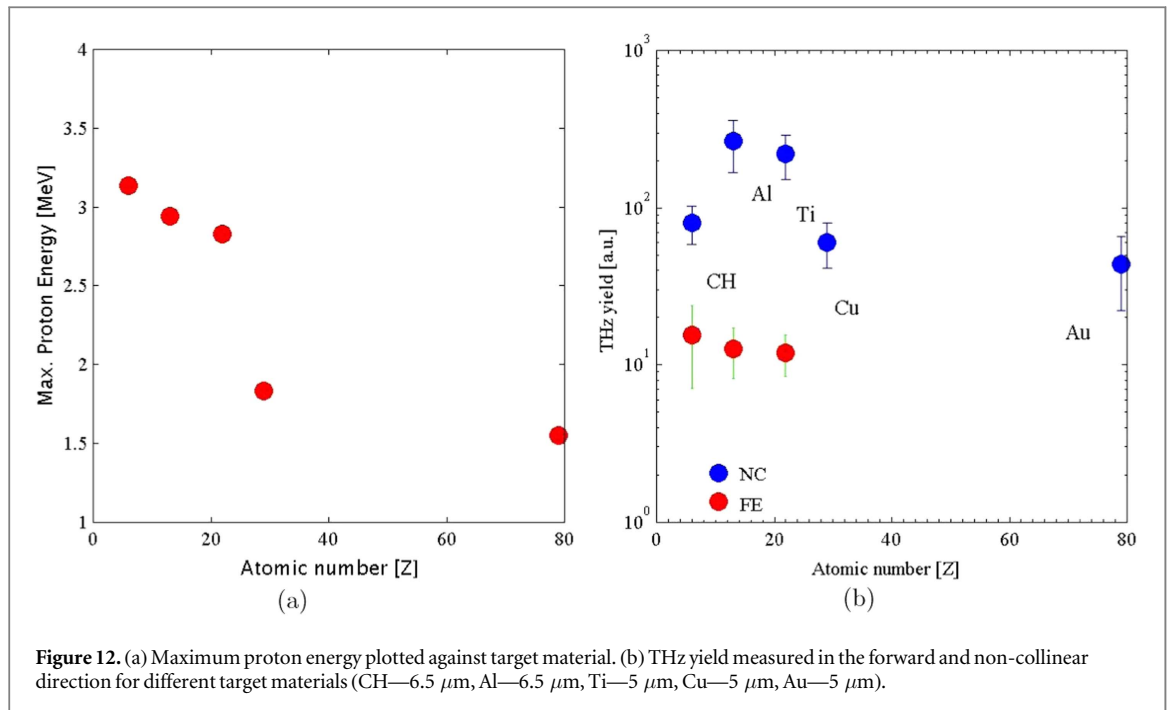
Figure 12. (a) Maximum proton energy plotted against target material. (b) THz yield measured in the forward and non-collinear direction for different target materials (CH—6.5 μm, Al—6.5 μm, Ti—5 μm, Cu—5 μm, Au—5 μm).
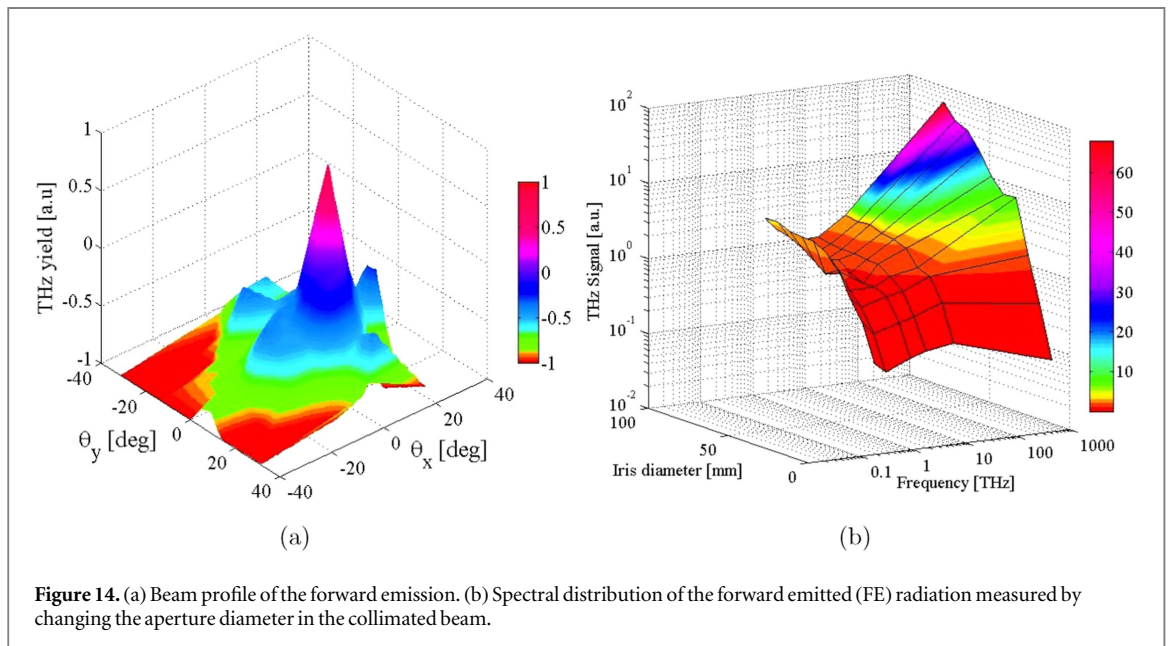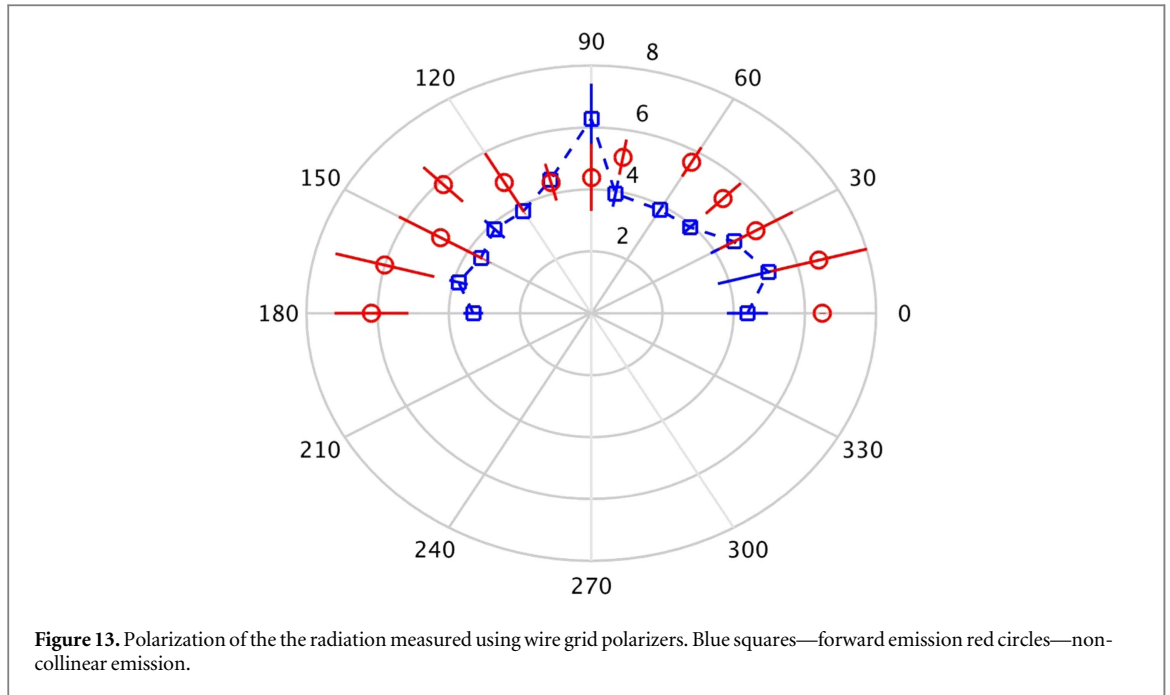
proton cut-off energy (figure 12(a)). Compared to dielectrics thin metals foils are a better alternative for terahertz generation. Although hydrocarbon impurities at the target rear surface are mostly accelerated during sheath acceleration process, it is the hot electrons which are generated at the front surface define the field dynamics at the rear. For comparable thickness, metals transport the electron beams from the front surface with minimal disruption [53] affecting the sheath field and thereby the acceleration process, resulting in higher THz yield in the non-collinear direction. On the other hand, forward emission does not vary significantly for target materials with comparable thicknesses.

4.4. Polarization measurements

Polarization of the emitted radiation is a great indicator of the emission process. The radiation emitted by sheath acceleration process and by TR should be radially polarized. We have measured the polarization using a broadband (0.9–75 THz) high extinction ratio (10^{-4}) wire grid polarizer [54] placed in front of the pyro detector. The polarizer was rotated in steps of 15° and the transmitted signal was recorded using the pyrometer. The results are plotted in figure 13. The signal strength of non-collinear emission was divided by a constant factor of 10 to plot the results in the same figure. In both cases the radiation is mostly radially polarized with small depolarization due to the shot to shot fluctuations. Simultaneous measurements of the ion spectra indicated that the fluctuations in the laser-target interaction process leads to weaker and less energetic ions as well as THz radiation in the non-collinear direction. We know that the thermal background or incoherent radiation is several orders of magnitude weaker than the coherent emission it should not contribute significantly to the measurements. Furthermore, calibration measurements of the beam collection and relay system at 800 nm provided the depolarization induced by the optics. Polarization measurements again substantiate theory of two main emission processes. TR and plasma sheath and ion acceleration process generating radially polarized THz radiation.

4.5. THz beam profile analysis—forward emission

The beam profile of the terahertz radiation emitted in the forward direction was recorded using aperture scanning technique. Since there are no large area detectors for broadband terahertz radiation, we used a beam profiler in the collimated terahertz beam and the transmitted energy was measured using the Pyrometer. The beam profiler consisted of a 10 × 10 cm metal plate with 1 × 1 cm hole. It was placed in the collimated 3 inch THz beam and moved in horizontal and vertical directions (perpendicular to the beam propagation direction). Multiple shots were taken at each position of the beam profiler to correct for the shot-to-shot fluctuations. The results are shown in figure 14(a). Here position (0°, 0°) is considered as the focus or target normal direction by the alignment laser. The central part of the alignment laser is transmitted to the ion spectrometer while the outer part was reflected by the THz collection and collimating parabola. For a perfect alignment, the laser propagation direction should be (45°, 0°) which is not collected by the OAP. Error bar of the order of 3° may arise from the physical positioning of the beam profiler with respect to the alignment laser. Although not symmetric with

Figure 13. Polarization of the the radiation measured using wire grid polarizers. Blue squares—forward emission red circles—non-collinear emission.

Figure 14. (a) Beam profile of the forward emission. (b) Spectral distribution of the forward emitted (FE) radiation measured by changing the aperture diameter in the collimated beam.

respect to the target normal $(0°, 0°)$ intense peaks due to TR of the electrons exiting the target rear are clearly visible around the focus surrounded by weaker background emission. Another strong peak is visible around $(7°, 7°)$ close to the laser propagation direction. It implies that a strong TR is emitted by the electrons which are pushed by the ponderomotive force of the laser in the propagation direction, similar to our observation in 2D PIC studies published previously [29]. In such a scenario, the two lobes of the TR should be on either side of the laser propagation direction. However, the other half of the peak is not collected by the forward emission collection optics. It is also evident that this peak is extremely localized meaning, the radiation is generated by highly energetic hot electrons. Moreover, the spectral content of this peak is dominated by high frequency components close to 2ω as shown in the figure 14(b). Further analysis of the EO signal in the FE should show the presence of multiple peaks. Furthermore, if the radiation is mainly emitted by the hot electrons coming out in the target normal direction, one would have expected low or signal free area along the target normal direction. However, we do not see a signal free area in the middle. Secondly, the signal strength should be symmetric on both sides of the target normal. As mentioned earlier, in addition to the strong CTR emission by the ponderomotively pushed electrons in the laser propagation direction, strong diffraction effects of the aperture could also contribute to the observed beam profile pattern.

Figure 14(b) presents the results of the spectrally resolved aperture scan. The aperture diameter was varied from 75 to 0 mm and in steps of 10 mm. The spectral content of the transmitted beam was measured using bandpass filters and pyroelectric detector. Similar to the beam profile measurements, strong emission is observed at large opening diameters of the aperture, substantiating the strong CTR emission laser propagation direction due to the ponderomotively pushed electrons. Furthermore, the spectral content is dominated by high frequency components suggesting that the emission is mostly TR. Although earlier studies have reported CTR in the optical regime [47], no THz radiation has been reported. However, the independent measurements based on EO and pyrometer suggests that though there are strong high frequency components ($2\omega_L$ and ω_L (laser frequency)), most of the emission is in the THz regime.

4.6. Proton spectra: dependence on incident laser pulse duration, target thickness and material

Even though proton acceleration was not the focus of our study, proton spectra was simultaneously recorded for every shot. This allowed us to compare the terahertz radiation to particle spectra and to understand the charge particle dynamics at the target rear surface during the interaction. The results presented in figures 11(a) and 12(a) are in agreement with previous studies published elsewhere [39, 55].

5. Conclusion

We have presented an extensive study on the high-power terahertz emission from the target rear surface during high-power laser–solid interaction. Radiation emitted mainly at large angles to the target normal direction and in the target normal direction were collected and investigated. Space-time integrated energy measurements and temporal and spectral measurements were carried out providing the pulse energy, duration, spectral content, polarization, angular beam profile. The experimental results were compared with the numerical model for terahertz generation. The space time integrated energy of the terahertz radiation measured for an incident laser pulse duration of 30 fs from a 5 μm thick Titanium foil was 712 μJ and 40 μJ in non-collinear and forward directions respectively. The measured spectral bandwidth of the forward emitted radiation is 275 THz where most of the energy is distributed in the high frequency regime. The pulse duration measurements using the non-collinear EO diagnostic indicated the generation of sub pico second THz pulses from the target rear surface with field strength 100 MV cm^{-1}. THz yield is greatly affected by the incident laser intensity. Laser intensity on target was altered either by varying the laser energy on target or by the pulse duration. The THz yield in the NC and FE directions increased with laser energy with a power law of $(I\lambda^2)^{1.45 \pm 0.12}$ and $(I\lambda^2)^{1.45 \pm 0.13}$. While the incident pulse duration has less effect on THz yield compared to energy for the same intensity range. This could be due to the fact that laser pulse duration affects the electron bunch duration, indicating the same energy is distributed over a longer electron bunch, thereby generating less THz. In both generation mechanism, the THz yield is proportional to the square of the particle energy and number. Hence shorter pulses are better candidate for THz generation using SR or CTR generation processes. Similarly low Z thinner targets are better candidates for THz generation like in the case of proton acceleration. EO measurements also validated the results from Pyroelectric detector and the emission is not isotropic. These results are also supported by the beam profile measurements presented in figure 14, where a strong emission is observed in the laser propagation direction. The background THz emission is generated by the electrons exiting the rear surface in target normal direction and a stronger TR emission is driven by the ponderomotively pushed electrons in the laser propagation direction. Polarization measurements in the NC and FE directions indicate that the THz generated at the rear surface is radially polarized.

Beyond the potential as a secondary radiation source, THz generation from the target rear surface can be employed as an inherent and non-invasive diagnostic to study the particle dynamics at the target rear surface during laser–solid interaction. THz yield could be employed as a direct estimate on the energy conversion from laser to the hot electrons. The non-collinear emission is proportional to the accelerated proton number and the TR yield could be compared to the electron number if a simultaneous measurement of the electron spectra is carried out. Future studies will focus on the detection of both electrons and ions from the rear surface. Nano-structured targets can be utilized to increase laser to hot electron energy conversion and thereby increase in proton number and energy resulting in higher THz yield.

Acknowledgments

References

[1] Macklin J J *et al* 1993 High-order harmonic generation using intense femtosecond pulses *Phys. Rev. Lett.* **70** 766

[2] Tatarakis M *et al* 2002 Laser technology: measuring huge magnetic fields *Nature* **415** 280

[3] Romagnani L *et al* 2005 Dynamics of electric fields driving laser acceleration of multi-MeV protons *Phys. Rev. Lett.* **95** 195001

[4] Leemans W P *et al* 2006 GeV electron beams from a centimeter-scale accelerator *Nat. Phys.* **2** 696

[5] Snavely R A *et al* 2000 Intense high-energy proton beams from PetaWatt laser irradiation of solids *Phys. Rev. Lett.* **85** 2945

[6] Hafez H A *et al* 2016 Intense terahertz radiation and their applications *J. Opt.* **18** 093004

[7] Gopal A *et al* 2013 Characterization of 700 μJ T rays generated during high-power laser solid interaction *Opt. Lett.* **38** 4705

[8] Liao G Q *et al* 2015 Bursts of terahertz radiation from large-scale plasmas irradiated by relativistic picosecond laser pulses *Phys. Rev. Lett.* **114** 255001

[9] Mousavi P *et al* 2009 Simultaneous composition and thickness measurement of paper using terahertz time-domain spectroscopy *Appl. Opt.* **48** 6541

[10] Kuehn W *et al* 2009 Phase-resolved two-dimensional spectroscopy based on collinear n-wave mixing in the ultrafast time domain *J. Chem. Phys.* **130** 164503

[11] Tudosa I *et al* 2004 The ultimate speed of magnetic switching in granular recording media *Nature* **428** 831–3

[12] Back C H *et al* 1998 Magnetization reversal in ultrashort magnetic field pulses *Phys. Rev. Lett.* **81** 3251–4

[13] Walkowski J and Münzenberg M 2016 Perspective: ultrafast magnetism and THz spintronics *J. Appl. Phys.* **120** 140901

[14] Wienholdt S *et al* 2012 THz switching of antiferromagnets and ferrimagnets *Phys. Rev. Lett.* **108** 247207

[15] Nicoletti D and Cavalleri A 2016 Nonlinear light–matter interaction at terahertz frequencies *Adv. Opt. Photonics* **8** 401

[16] Hirori H *et al* 2011 Extraordinary carrier multiplication gated by a picosecond electric field pulse *Nat. Commun.* **2** 594

[17] Nanni E A *et al* 2015 Terahertz-driven linear electron acceleration *Nat. Commun.* **6** 8486

[18] Lundh O *et al* 2011 Few femtosecond, few kilo ampere electron bunch produced by a laser-plasma accelerator *Nat. Phys.* **7** 219

[19] Berden G *et al* 2004 Electro-optic technique with improved time resolution for real-time, nondestructive, single-shot measurements of femtosecond electron bunch profiles *Phys. Rev. Lett.* **93** 114802

[20] van Tilborg J *et al* 2006 THz radiation as a bunch diagnostic for laser-wakefield-accelerated electron bunches *Phys. Plasmas* **13** 056704

[21] Hoffmann M C and Fúlóp J A 2011 Intense ultrashort terahertz pulses:generation and applications *J. Phys. D: Appl. Phys* **44** 083001

[22] Gibbon P 2005 *Short Pulse Laser Interactions with Matter* (London: Imperial College Press)

[23] Li C *et al* 2011 Effects of laser-plasma interactions on terahertz radiation from solid targets irradiated by ultrashort intense laser pulses *Phys. Rev.* E **84** 036405

[24] Sagisaka A *et al* 2008 Simultaneous generation of a proton beam and terahertz radiation in high-intensity laser and thin foil interaction *App. Phys.* B **90** 373

[25] Hamster H *et al* 1993 Sub-picosecond, electromagnetic pulses from intense laser plasma interaction *Phys. Rev. Lett.* **71** 2725–8

[26] Zhou H B *et al* 2017 Terahertz generation from laser-driven ultrafast current propagation along a wire target *Phys. Rev.* E **95** 013201

[27] Li C *et al* 2016 Backward terahertz radiation from intense laser-solid interactions *Opt. Exp.* **24** 4010

[28] Li C *et al* 2014 Role of resonance absorption in terahertz radiation generation from solid targets *Opt. Exp.* **22** 11797

[29] Gopal A *et al* 2012 Observation of energetic no-collinear THz pulses from relativistic solid density plasmas *New J. Phys.* **14** 083012

[30] Gopal A *et al* 2013 Observation of gigawatt-class THz pulses from a compact laser-driven particle accelerator *Phys. Rev. Lett.* **111** 074802

[31] Herzer S *et al* An analytical model for the terahertz emission from solid density laser produced plasmas (submitted)

[32] Liao G Q *et al* 2015 Demonstration of coherent terahertz transition radiation from relativistic laser–solid interactions *Phys. Rev. Lett.* **114** 255001

[33] Liao G Q *et al* 2017 Intense terahertz radiation from relativistic laser-plasma interactions *Plasma Phys. Control. Fusion* **59** 014039

[34] Jin Z *et al* 2016 Highly efficient terahertz radiation from a thin foil irradiated by a high-contrast laser pulse *Phys. Rev.* E **94** 033206

[35] Wilks S C *et al* 2001 Energetic proton generation in ultra-intense laser-solid interactions *Phys. Plasmas* **8** 542

[36] Mora P 2003 Plasma expansion into a vacuum *Phys. Rev. Lett.* **90** 185002

[37] Betti S *et al* 2005 Expansion of a finite-size plasma in vacuum *Plasma Phys. Control. Fusion* **47** 521

[38] Schreiber J *et al* 2006 Analytical model for ion acceleration by high-intensity laser pulses *Phys. Rev. Lett.* **97** 045005

[39] Fuchs J *et al* 2006 Laser-driven proton scaling laws and new paths towards energy increase *Nat. Phys.* **2** 48–54

[40] Jackson J D 1999 *Classical Electrodynamics* 3rd edn (New York: Wiley) ch 14

[41] Frank I M and Ginzburg V L 1945 *J. Phys. USSR* **9** 35

[42] Santos J J *et al* 2002 Fast electron transport in ultra intense laser pulse interaction with solid targets by rear-side self-radiation diagnostics *Phys. Rev. Lett.* **89** 025001

[43] Zheng J *et al* 2002 Spectrum of transition radiation from hot electrons generated in ultra-intense laser plasma interaction *Phys. Plasmas* **9** 3610

[44] Zheng J *et al* 2003 Theoretical study of transition radiation from hot electrons generated in the laser–solid interaction *Phys. Plasmas* **10** 2994

[45] Baton S D *et al* 2003 Evidence of ultrashort electron bunches in laser-plasma interactions at relativistic intensities *Phys. Rev. Lett.* **91** 105001

[46] Popescu H *et al* 2005 Sub femtosecond, coherent, relativistic, and ballistic electron bunches generated at ω_0 and $2\omega_0$ in high intensity laser-matter interaction *Phys. Plasmas* **12** 063106

[47] Bellei C *et al* 2010 Micron-scale fast electron filaments and recirculation determined from rear-side optical emission in high-intensity laser-solid interactions *New J. Phys.* **12** 073016

[48] Jaeckel O *et al* 2010 All-optical measurement of the hot electron sheath driving laser ion acceleration from thin foils *New J. Phys.* **12** 103027

[49] Shan J-P *et al* 2000 Single-shot measurement of terahertz electromagnetic pulses by use of electro-optic sampling *Opt. Lett.* **25** 426

[50] Casalbuoni A *et al* 2009 Ultra broadband terahertz source and beamline based on coherent transition radiation *Phys. Rev. Spec. Top. Accel. Beams* **12** 030705

[51] Schwoerer H *et al* 2006 Laser-plasma acceleration of quasi-monoenergetic protons from microstructured targets *Nature* **439** 445–8

[52] Ceccotti T *et al* 2007 Proton acceleration with high-intensity ultrahigh-contrast laser pulses *Phys. Rev. Lett.* **99** 185002

[53] Fuchs J *et al* 2003 Spatial uniformity of laser-accelerated ultrahigh-current mev electron propagation in metals and insulators *Phys. Rev. Lett.* **91** 255002

[54] High Contrast Infrared Polarizers for for the mm-waves, THz, FIR and MIR region (http://infraspecs.de)

[55] Zeil K *et al* 2010 The scaling of proton energies in ultrashort pulse laser plasma acceleration *New J. Phys.* **12** 045015

15